# Impedance Stability of Single-Phase *LCL* Grid-Connected Voltage Source Inverters with Wideband Gap Devices Under Different Control Approaches

Ramy Ali, Terence O'Donnell
UNIVERSITY COLLEGE DUBLIN
Dublin, Ireland
E-Mail: ramy.ali@ucdconnect.ie, terence.odonnell@ucd.ie

## Acknowledgements

This work has emanated from research conducted with the financial support of Science Foundation Ireland under Grant No. SFI/16/IA/4496. The opinions, findings, and conclusions or recommendations expressed in this material are those of the authors and do not necessarily reflect the views of the Science Foundation Ireland.

## Keywords

« Wide bandgap devices (WBG) », « Voltage Source Inverter (VSI) », « *LCL*-type inverter », « Impedance model », « Stability analysis ».

## Abstract

This paper discusses the impedance stability of the grid connected VSI that is built using wide bandgap (WBG), SiC, or GaN semiconductors devices. The use of WBG devices have the benefits of higher switching frequency, lower losses, and smaller size. The impedance stability of the WBG-based VSI is studied under both grid side and inverter side current control. The impedance model of the VSI is developed and validated in Matlab/Simulink. Using this model, the variation of the VSI output impedance at increased switching frequencies is studied. The impedance stability is examined for the case where the VSI is connected at different points in a distribution network. The CIGRE European benchmark LV network is used. The analysis reveals that the impedance stability of the grid-side current-controlled WBG-based VSI is improved at higher switching frequencies. Simulation results are provided for verifying the theoretical analysis.

## Introduction

Recently, with the motivation of improving efficiency and reducing the footprint of the voltage source inverter (VSI), the wide bandgap (WBG) semiconductors materials such as SiC, GaN have been adopted in the grid connected VSI. These devices have the potential to offer a smaller size, higher switching frequency, better reliability, and superior efficiency than the conventional silicon-based switches [1]. Although clearly of advantage in the VSI, it is of interest to also ask if this move to higher switching frequencies might have stability or power quality implications for the power system, especially in the context of high inverter-based resources (IBR) penetration levels.

Typically, the different stability concerns of the grid connected VSI have been investigated using one of two approaches: the state-space method in the time domain or the impedance-based method in the frequency domain. The state-space approach depends on the identification of the eigenvalues of the system which requires a detailed description of the system parameters. In contrast, the impedance-based method is a powerful approach as it evaluates the stability of a given converter based on its terminal characteristics. It essentially characterizes the VSI as a current source in parallel with an impedance, and the grid it connects to as voltage source in series with an impedance. The VSI-grid system is stable if ratio of the grid impedance $Z_g$ to the inverter output impedance $Z_o$ satisfies the Nyquist stability criterion (NSC) [2].

The grid connected VSI is typically equipped with an *LCL* filter to reduce the PWM switching harmonics. The output impedance $Z_o$ of the grid connected VSI is a frequency dependent impedance as various control loops govern its properties [3]. As different control loops are effective in different frequency ranges, the output impedance characteristic varies across a wide frequency range. For instance, slower control loops, such as the dc link/power control loop, in addition to the phase locked loop (PLL), shape the low frequency behavior of the output impedance. The current control loop, on the other hand, has a larger bandwidth and dominates the medium-to-high frequency area of the output impedance. The *LCL* filter parameters determine the high frequency characteristic of the VSI output impedance [4]. On the other side, the grid impedance $Z_g$ is also a frequency-dependent impedance and characterized by the impedance of long transmission lines/cables, transformers, and loads. Therefore, the interaction between both frequency-dependent impedances might occur and lead to harmonic resonances and instability problems over a wide range of frequencies from few Hertz (Hz) to several kilohertz (kHz).

Deploying WBG devices in the VSI results in a substantially higher switching frequency of operation, and the *LCL* filter parameters and the current controller bandwidth will be affected as they are dependent on the switching frequency. The switching frequency of the VSI has a significant impact on the crossover frequency ($f_c$) and thus the bandwidth of the current controller as it is usually designed to be in the range of $[f_{sw}/40, f_{sw}/5]$ [5]. As previously stated, the current controller bandwidth affects the characteristics of the VSI output impedance, therefore the current controller is a major control loop that could produce impedance stability issues in the VSI-grid system in the medium to high frequency range.

For the current control loop, the control target of the *LCL* grid-connected VSI can be the inverter-side current feedback (ICF) or the grid-side current feedback (GCF) [6]. Both choices have pros and cons. For instance, the ICF offers a more cost-effective option because the current sensor on the inverter-side of the VSI may be used for both overcurrent protection and control [7]. The ICF, on the other hand, is hampered by its inability to control the power factor on the grid [8]. Even though the GCF has the advantage of directly managing the power injected into the grid, ensuring the power factor of the grid, it requires an additional current sensor, which adds to the total cost of the system.

This work investigates the impact of the use of WBG devices and the consequent increase in switching frequency on the impedance stability of the VSI under both inverter side and grid side current control approaches. Although other works have studied the relative stability of both the ICF and GCF control approaches using the root locus method [9], these studies were conducted for the relativity lower switching frequencies of conventional silicon switches [4] and did not consider the impedance stability. This work investigates whether the impedance stability issues are likely to be more or less of an issue as VSI switching frequencies increase.

## Modeling of VSI System

The configuration of a single-phase grid connected VSI, and its control system is depicted in Fig. 1. The VSI is composed of a full bridge DC-AC inverter that is supplied from a dc voltage source $U_{dc}$, which should be always higher than the peak ac voltage to generate the inverter output voltage, $u_i$. The VSI is connected to an *LCL* filter to damp the PWM switching harmonics, where $L_1$ is the inverter-side inductor, $C_f$ is the filter capacitor, $R_d$ is the passive damping resistor, and $L_2$ is the grid-side inductor. Generally, the inverter-side inductor $L_1$ is designed to achieve

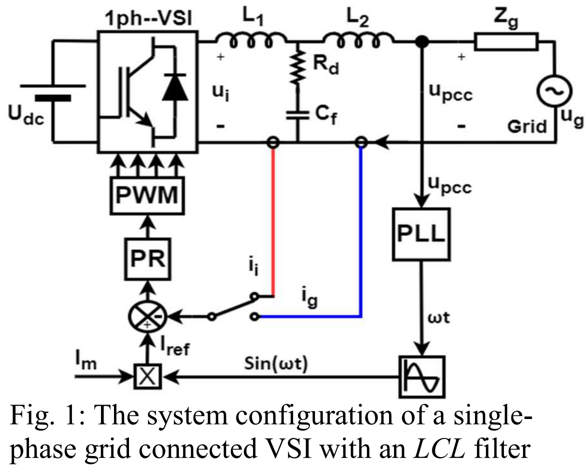

Fig. 1: The system configuration of a single-phase grid connected VSI with an *LCL* filter employing PR controller

maximum allowable output current ripple of 20-30% of the rated output current [10]. The filter capacitor $C_f$ is chosen as a compromise between high-frequency harmonic attenuation and reactive power consumption at the fundamental frequency. For low- and medium-power VSI, the permitted reactive power of the capacitor is typically in the range of 2% to 15% of the rated power [11]. The damping resistance is usually designed to be around one-third of the capacitive reactance at the *LCL* resonance frequency [12]. Lastly, the grid-side inductor $L_2$ is set to comply with the grid code on VSI harmonic emission. It is usually selected to achieve a maximum harmonic attenuation rate of 20%. The value of $L_2$ is a trade-off between the filter cost and the total harmonic distortion (THD) of the grid current [13].

The low voltage (LV) network at the point of common coupling (PCC) in Fig. 1 is represented by an ideal voltage source $u_g$ in series with a grid impedance $Z_g$, which depends on the type of grid, e.g., cable or overhead lines, urban or rural, etc. The PCC voltage is fed to the PLL which captures the voltage phase angle to generate the sinusoidal reference current $I_{ref}$ of the current control loop. In this work, the injected grid current is controlled in the stationary reference frame ($\alpha\beta$ frame), so a proportional-resonance (PR) controller is employed which shows a more robust performance [14]. It is worth mentioning that in this work, a passive damping for the intrinsic *LCL* filter resonance [15] is used for the sake of simplicity. To analyze the stability of the VSI-grid system using the impedance-based stability approach, a linearized, small-signal, model of the VSI should be developed. Furthermore, the grid impedance of the LV network where the VSI is connected should also be evaluated to assess the VSI-grid system stability.

## Small Signal Impedance Model of the VSI

The impedance stability study is performed using the impedance model of the *LCL* grid connected VSI, which is based on inverter-side current feedback (ICF) and grid-side current feedback (GCF). This model is mathematically created and validated using a Matlab/Simulink-based test system. Fig. 2 shows the control block diagram for both ICF and GCF.

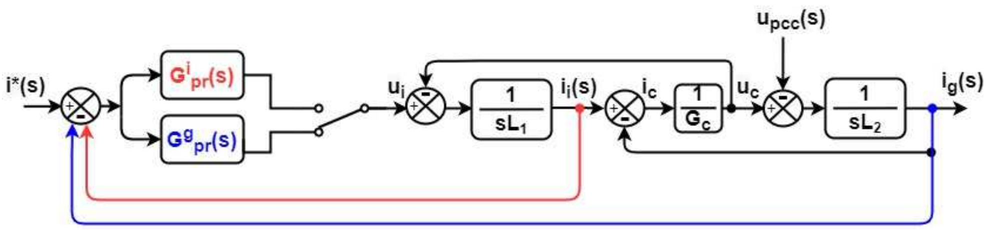


Fig. 2: Control block of *LCL* grid connected VSI with ICF (Red) and GCF (Blue).

To distinguish between the ICF and GCF controllers, $G^i_{pr}$ is used for ICF, and $G^g_{pr}$ for the GCF. In Fig. 2, $G_{pr}$ represents the transfer function of the PR controller which can be written as in (1), where $k_p$ is the proportional gain, and $k_r$ is the resonant integral gain.

$$G_{pr} = k_p + k_r \frac{2\omega_{co}s}{s^2+2\omega_{co}s+\omega_g^2} \quad (1)$$

Furthermore, the instability caused by infinite gain at the nominal grid frequency $\omega_g$ can be avoided by choosing a cut-off frequency, $\omega_{co}$ that is substantially lower than the nominal grid frequency ($\omega_{co} \ll \omega_g$) [16]. To simplify the study, the parasitic resistances of the *LCL* filter's inductors are omitted, which also corresponds to the worst working circumstances of the filter. It is also assumed that any impact of the self-resonant frequency (SRF) of the inductor can be neglected in the frequency range of interest. Typically, the SRF of the inductor occurs in the MHz to GHz range [17] and is lower for higher inductance, lower current devices which is not the case here.

The current controller gains ($k_p, k_r$) can be fine-tuned using the PID tuner app in Matlab/Simulink, or they can be estimated mathematically with some efforts for fine-tuning. Because the crossover frequency

($f_c$) is lower than the resonance frequency of the *LCL* filter, the influence of the *LCL* filter capacitor can be ignored when calculating the open loop gain at frequencies less than or equal to $f_c$, and the transfer function of the PR controller can be approximated to $k_p$ at higher or equal to $f_c$ [18]. Here the design of the GCF controller gains is given as an example to illustrate the design approach. The open loop gain of the GCF can be expressed as:

$$T_{GCF}(s) = G_{pr}^{g} \cdot \frac{1}{s^2 L_1 L_2 G_c + (L_1 + L_2)s} \tag{2}$$

The amplitude of $T_{GCF}(s)$ at $f_c$ is unity, so the $|T_{GCF}(j\omega_c)|$ can be depicted as:

$$|T_{GCF}(j\omega_c)| = \left|\frac{k_p}{j\omega_c(L_1 + L_2)}\right| = 1,$$

$$k_p = \omega_c(L_1 + L_2) \tag{3}$$

Furthermore, the resonant gain ($k_r$) can be estimated as in [19]:

$$k_r = \frac{k_p \cdot \omega_c}{10} \tag{4}$$

where, $\omega_c = 2\pi f_c$ and the $f_c$ is usually selected to be one-tenth of the switching frequency $f_{sw}$ ($f_c = \frac{1}{10} f_{sw}$). It is worth highlighting that $k_p$, $k_r$ values generated from (4) and (5) are estimates that may need to be fine-tuned.

Further, the equivalent transfer function of the filter capacitor branch $G_c$ can be expressed in (5)

$$G_c = \frac{s\, C_f}{1 + s\, C_f R_d} \tag{5}$$

The inverter output impedance $Z_o$ is measured at the PCC in Fig. 1 for both control choices, ICF and GCF, for the sake of comparability. Therefore, $Z_o$ can be calculated by ignoring the input reference signal in Fig. 2 and calculating the ratio of $u_{pcc}(s)$ and $i_g(s)$ as $i_i(s)$ is the feedback signal (the red arrow).

The expression of the inverter output impedance $Z_o^i$ for the ICF can be calculated as:

$$Z_o^i = \frac{u_{pcc}(s)}{-i_g(s)} = \frac{s^2 L_1 L_2 G_c + s L_2 G_c G_{pr}^i + s(L_1 + L_2) + G_{pr}^i}{s L_1 G_c + G_c G_{pr}^i + 1} \tag{6}$$

The VSI with GCF controller is analyzed using the same setup in Fig. 1 by using $i_g$(s) as a feedback signal (the blue arrow). According to the control block diagram shown in Fig. 2, the expression of the output impedance of the VSI-based GCF, $Z_o^g$ can be expressed as:

$$Z_o^g = \frac{u_{pcc}(s)}{-i_g(s)} = \frac{s^2 L_1 L_2 G_c + s(L_1 + L_2) + G_{pr}^g}{s L_1 G_c + 1} \tag{7}$$

To assess the impedance stability of the *LCL* grid connected VSI for the higher switching frequencies associated with the use of wide bandgap semiconductors, the rated data of the VSI, *LCL* filter parameters and current controller gains at different switching frequencies as well as the grid impedances at the point of connection to the grid are listed in Table I. It is worth mentioning that the current controllers have been designed to have a cross-over frequency of one-tenth of the switching frequency for ICF and GCF.

**Table I: VSI rated data, *LCL* filter parameters, current controller gains, and the grid impedances**

| Parameter | Symbol | Switching Frequency | | | |
|---|---|---|---|---|---|
| | | 10 kHz | 20 kHz | 50 kHz | 100 kHz |
| Rated Power | $P_{\mathrm{o}}$ | 5 kW | | | |
| DC link Voltage | $U_{\mathrm{dc}}$ | 400 V | | | |
| Grid voltage | $U_{\mathrm{g}}$ | 230 V | | | |
| Grid frequency | $f_{\mathrm{g}}$ | 50 Hz | | | |
| Inverter-side Inductor | $L_1$ | 2.6 mH | 1.3 mH | 0.52 mH | 0.26 mH |
| Grid-side Inductor | $L_2$ | 0.65 mH | 0.33 mH | 0.13 mH | 0.065 mH |
| Filter Capacitor | $C_{\mathrm{f}}$ | 5 µf | 5 µf | 5 µf | 5 µf |
| Damping resistor | $R_{\mathrm{d}}$ | 3.5 Ω | 3.5 Ω | 3.5 Ω | 3.5 Ω |
| PR controller gains of ICF | $k_p^i, k_r^i, \omega_{co}$ | 21, 2310, 0.5 | 21.7, 4781, 0.5 | 23, 8988, 0.5 | 20, 1.9e4, 0.5 |
| PR controller gains of GCF | $k_p^g, k_r^g, \omega_{co}$ | 18.4, 2017, 0.5 | 16.4, 3616, 0.5 | 13, 7224, 0.5 | 15, 1.6e4, 0.5 |
| $Z_g$ at Bus 1 | $R_g^{B1}, L_g^{B1}$ | 0.06 Ω, 0.35 mH | | | |
| $Z_g$ at Bus 2 | $R_g^{B2}, L_g^{B2}$ | 0.13 Ω, 0.76 mH | | | |

Furthermore, a test system constructed in Matlab/Simulink is used to validate the analytical formula for the small-signal output impedance of both ICF and GCF based VSI. The test system includes a disturbance voltage source in series with the grid voltage, as well as the entire switching model of the grid connected VSI. The disturbance voltage has an amplitude of 8% of the rated voltage and is swept across a wide frequency range of 5 Hz to 10 kHz with a resolution of 5 Hz. A Fourier analysis is used to collect both the terminal voltage and injected current at each frequency of disturbance to determine the impedance at that frequency. The impedance acquired in this approach is then compared to that obtained using the analytical formulas in (6) and (7). The magnitude and phase graphs that result from the validation of ICF and GCF, respectively, are shown in Fig. 3 and Fig. 4. This validation considers the filter parameters and current controller gains at a switching frequency of 10 kHz. The magnitude and phase graphs are comparable with the theoretical estimates except in the low frequency area around 50 Hz. This is because removing the fundamental frequency component's effect from the test system in Matlab/Simulink is challenging, especially when the current value at 50 Hz is high.

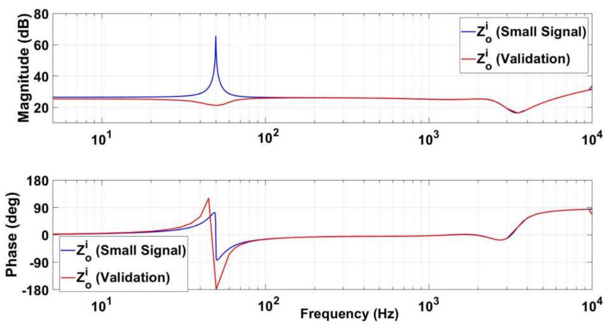


Fig. 3: Small-signal and validation of $Z_o^i$ at $f_{sw}$=10 kHz

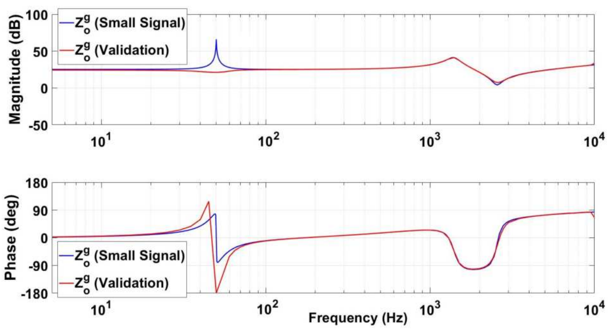


Fig. 4: Small-signal and validation of $Z_o^g$ at $f_{sw}$=10 kHz

## Output Impedance of WBG based VSI

The WBG-based VSI operates at a substantially greater switching frequency ($f_{sw} \geq 50$ kHz) than the traditional silicon-based inverter, which operates at a switching frequency of up to 10 kHz [19]. To analyze the impedance stability of the VSI-grid system, the VSI output impedance, for both ICF and GCF, will be examined over various switching frequencies that are typically used in silicon-based and WBG-based VSI. Fig. 5 shows the frequency response of VSI output impedance, $Z_o^i$ at various switching frequencies. The phase plot of the ICF-based VSI never crosses the -90° phase, indicating that it is stable at different switching frequencies. The phase angle, on the other hand, approaches a deeper lag as the switching frequency rises, implying that the impedance stability of the grid connected VSI suffers as the switching frequency rises. In contrast, as the switching frequency increases, $Z_o^g$ gains more damping because the phase plot at the magnitude dip moves further away from the -90° limit, as shown in Fig. 6.

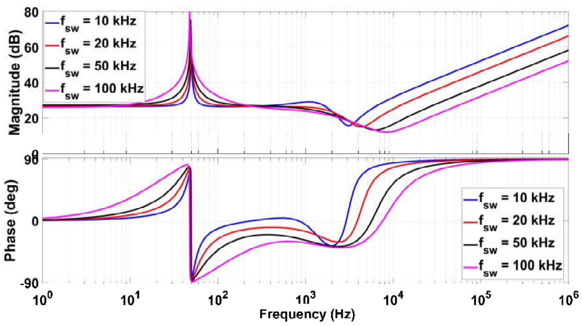


Fig. 5: Bode plots of $Z_o^i$ at different $f_{sw}$

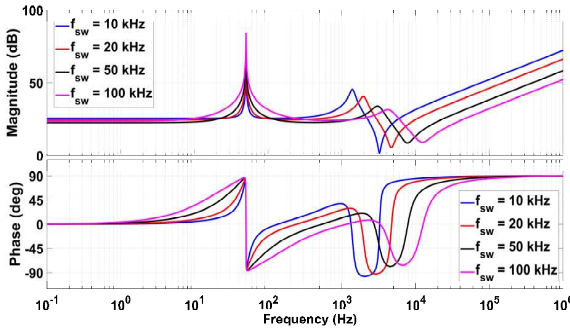


Fig. 6: Bode plots of $Z_o^g$ at different $f_{sw}$

## Study Cases of Impedance Stability and Power Quality Issues of the ICF and GCF based VSI in the LV Distribution Grid

Because the LV distribution network is mostly a radial system, the grid to which the VSI is connected has varying grid impedances, $Z_g$, depending on the distance between the connection point and the MV transformer. As a result, the VSI output impedance may interact with the multiple grid impedances, causing the VSI-grid system to become unstable. The grid impedance is determined in this study using the CIGRE European benchmark LV network [20], [21] shown in Fig. 7, where the impedance at the closest, bus B1, and the farthest, bus B2, points to the MV transformer are evaluated and listed in Table I.

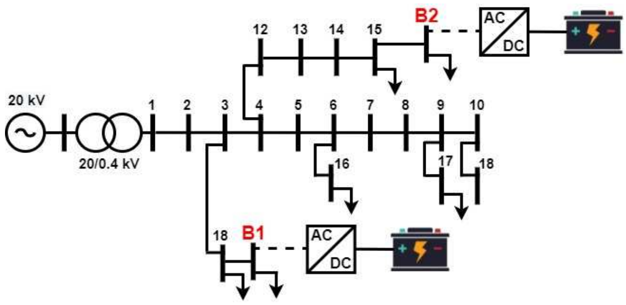


Fig. 7: The single line diagram of the CIGRE LV distribution feeder.

The ICF-based VSI is still more stable than the GCF, but its phase plot has less damping at high frequencies. On the other hand, the GCF-based VSI acquires better impedance stability at higher switching frequencies, as seen in the preceding analysis. Therefore, the case studies in this section will only look at the GCF-based VSI to demonstrate its improved impedance stability at higher switching frequencies. Furthermore, the highest grid impedance is found at the farthest point from the MV transformer, at bus B2, which reflects the worst-case scenario that could jeopardize the stability of the VSI-grid system. As a result, this is the only case considered in this study.

As mentioned earlier, the Nyquist stability criterion (NSC) can be employed to examine the stability of VSI-grid system based on the ratio of the grid impedance $Z_g$ to the inverter output impedance $Z_o$. However, the NSC is a relative measure for the VSI-grid system's stability. Hence, the frequency response, Bode plot, of both the VSI output impedance and the grid impedance can be used to obtain an absolute norm of the VSI-grid system stability. When assessing the impedance stability of the VSI-grid system, two crucial points in the Bode plots of both impedances should be observed [22]:

1. The intersection points of the inverter output impedance $Z_o$ and the grid impedance $Z_g$ magnitude curves, which represent the zero-dB crossing points (resonance frequency) as both impedances have the same magnitude.
2. The phase margin angle $\varphi_{PM}$ at the intersection point of $Z_o$ and $Z_g$ which can be calculated as $\varphi_{PM} = 180 - [\varphi_{Z_g} - \varphi_{Z_o}]$, where $\varphi_{Z_o}$ and $\varphi_{Z_g}$ are the phase angle of the inverter output impedance and the grid impedance respectively. A positive phase margin angle ensures the stability of the VSI-grid system [23].

The interaction between the VSI and the grid is analyzed using the VSI output impedance $Z_o$ and the grid impedance $Z_g$, as shown in Fig. 8. The Bode plot in Fig. 8 predicts the instability of the injected grid current $I_g$ of the VSI-based GCF with $f_{sw}$= 10 kHz because the phase margin angle at the resonance frequency of 2440 Hz is negative, -2.8°. As a result, as shown in Fig. 9(a), the injected grid current $I_g$ is substantially distorted, and the harmonic spectrum of $I_g$ in Fig. 9(b) is dominated by the resonance frequency at zero-dB crossing of $Z_o^g$ and $Z_g$. The grid current $I_g$ of the GCF based VSI with $f_{sw}$= 50 kHz, on the other hand, remains stable because the phase margin angle at the resonance frequency of 4140 Hz is positive, +13° as seen in the Bode plot in Fig. 8. The simulation findings in Fig. 10(a) and the harmonic spectrum of $I_g$ in Fig. 10(b) both support this conclusion.

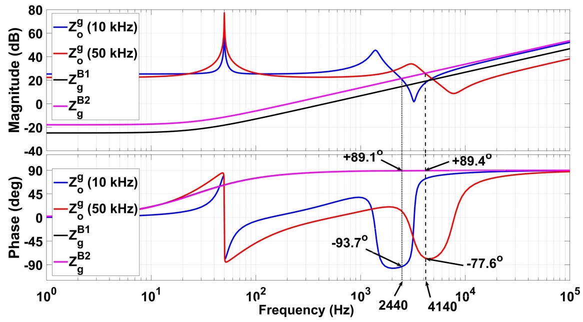

Fig. 8: Bode plot of $Z_o^g$ at different $f_{sw}$ and connected to $Z_g$ at bus B1 and bus B2.

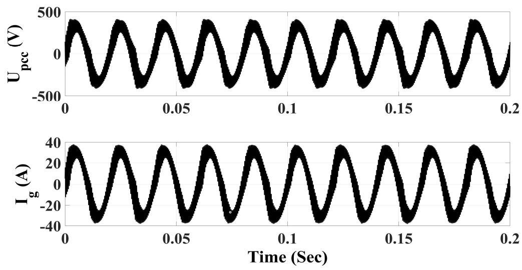

(a)

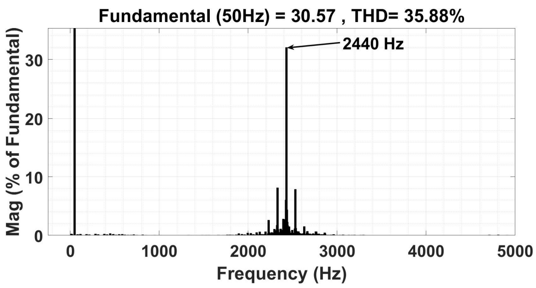

(b)

Fig. 9: Simulation results of VSI with $f_{sw}$=10 kHz connected to bus B2. (a) $U_{pcc}$ and $I_g$ waveforms (b) Harmonic spectrum of $I_g$.

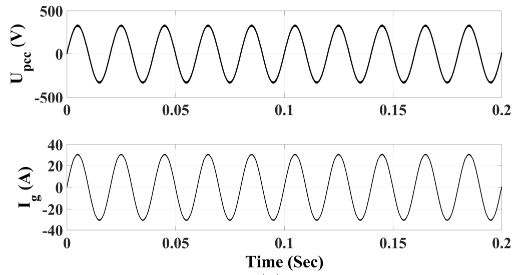

(a)

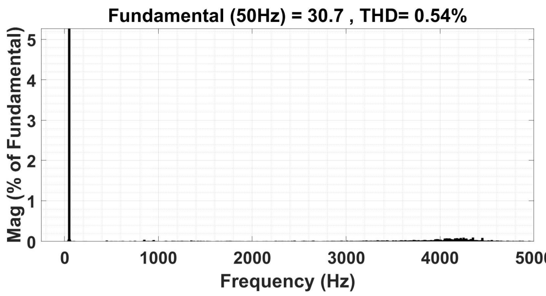

(b)

Fig. 10: Simulation results of VSI with $f_{sw}$=50 kHz connected to bus B2. (a) $U_{pcc}$ and $I_g$ waveforms (b) Harmonic spectrum of $I_g$

Further case study is depicted in Fig. 11, where the VSI operates at $f_{sw}$= 20 kHz and $f_{sw}$= 100 kHz. The output impedance of the grid connected VSI, $Z_o^g$ and the grid impedance, $Z_g$ are used to test the system stability. According to the Bode plot in Fig. 11, the grid tied VSI is unstable when works at $f_{sw}$= 20 kHz and connected at bus B2, because the phase margin angle is negative, -0.4° at the resonance frequency of 3070 Hz.

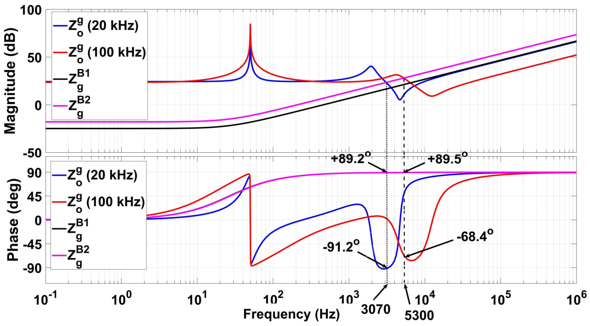


Fig. 11: Frequency response of $Z_o^g$ at various $f_{sw}$ and the VSI is connected at bus B1 and bus B2.

Therefore, as shown in Fig. 12, the injected grid current $I_g$ of the VSI-based GCF with $f_{sw}$= 20 kHz is unstable. Further, as depicted in Fig. 12(b), the harmonic spectrum is dominated by the resonance frequency. In contrast, when the switching frequency $f_{sw}$ is raised to 100 kHz, the stability of the grid connected VSI improves significantly because the phase margin angle is positive, +22.1° at the resonance frequency of 5300 Hz. As a result, the VSI-grid system has enough damping to attenuate the resonance frequency while maintaining the stability. The injected grid current $I_g$ is perfect as shown in Fig. 13(a), and the harmonic spectrum of $I_g$ in Fig. 13(b) has an acceptable power quality level.

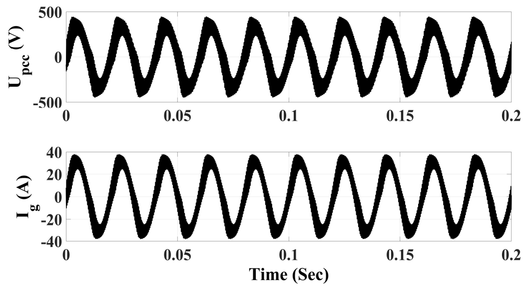


(a)

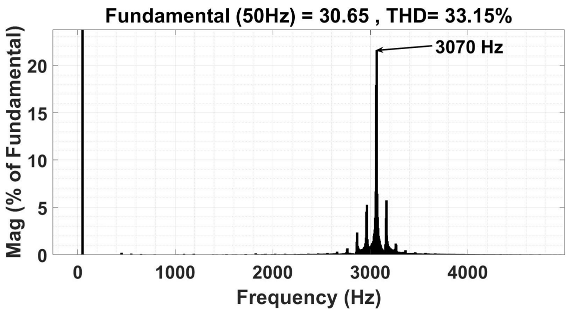


(b)

Fig. 12.: Simulation results of VSI with $f_{sw}$=20 kHz connected to bus B2. (a) $U_{pcc}$ and $I_g$ waveforms (b) Harmonic spectrum of $I_g$.

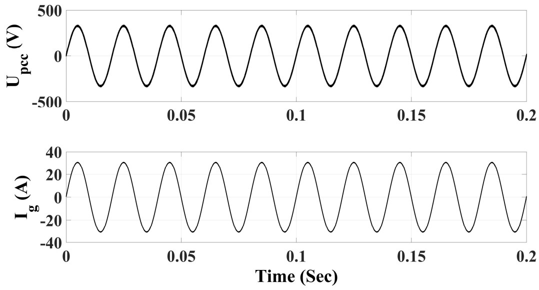


(a)

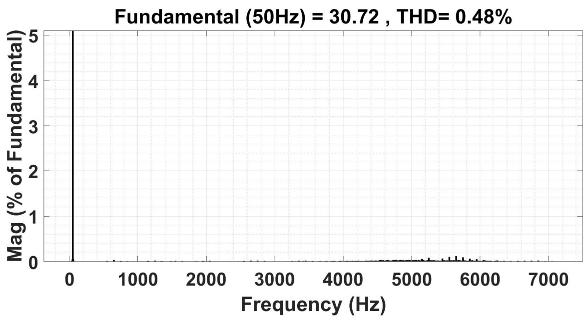


(b)

Fig. 13.: Simulation results of VSI with $f_{sw}$=100 kHz connected to bus B2. (a) $U_{pcc}$ and $I_g$ waveforms (b) Harmonic spectrum of $I_g$

## Conclusion

The impedance stability of the WBG-based grid-connected VSI, which operates at higher switching frequencies, is explored at various points within the LV network. In Matlab/Simulink, the analytical expression of the VSI output impedance under both inverter-side and grid-side current control approaches is developed by using the small signal model of the single phase *LCL* grid connected inverter and the impedance expressions are validated by utilizing a test system that is constructed in Matlab/Simulink. The analysis and diverse study situations reveal that the impedance stability of the VSI-grid system is improved for GCF-based VSI at higher switching frequencies. The VSI-grid system obtains higher damping at higher switching frequencies, which ensures the stability of the grid connected inverter while also enhancing the quality of the injected grid current.

## References


[1] Singh S.: Recent Advancements in Wide Band Semiconductors (SiC and GaN) Technology for Future Devices, Silicon 2021, pp. 1–8.

[2] Amin M.: Small-Signal Stability Assessment of Power Electronics Based Power Systems: A Discussion of Impedance-and Eigenvalue-Based Methods, IEEE Transactions on Industry Applications, vol. 53, no. 5, pp. 1–17, Sep. 2017.

[3] Ali R.: Parameters Influencing Harmonic Stability for Single-phase Inverter in the Low Voltage Distribution Network, Proc. 2021 IEEE PES Innov. Smart Grid Technol. Eur. Smart Grids Towar. a Carbon-Free Futur. ISGT Eur. 2021, pp. 1–5, 2021.

[4] Yu Y.: Modeling and analysis of resonance in LCL-type grid-connected inverters under different control schemes," *Energies*, vol. 10, no. 1, 2017.

[5] Bao C.: Step-by-step controller design for LCL-Type Grid-Connected inverter with capacitor-current-feedback active-damping," IEEE Trans. Power Electron., vol. 29, no. 3, pp. 1239–1253, 2014.

[6] Zheng C.: The Interaction Stability Analysis of a Multi-Inverter System Containing Different Types of Inverters, Energies 2018, vol. 11, no. 9.

[7] Pan D.: Analysis and Design of Current Control Schemes for LCL-Type Grid-Connected Inverter Based on a General Mathematical Model, IEEE Transactions on Power Electronics, vol. 32, no. 6, pp.–16, Jun. 2017.

[8] Zhou X.: A novel inverter-side current control method of LCL-Filtered inverters based on high-pass-filtered capacitor voltage feedforward, IEEE Access, vol. 8, pp. 1-11, 2020.

[9] Dannehl J.: Limitations of voltage-oriented PI current control of grid-connected PWM rectifiers with LCL filters, IEEE Transactions on Industrial Electronics, vol. 56, no. 2, pp. 1-9, 2009.

[10] Han Y.: Modeling and stability analysis of LCL-type grid-connected inverters: A comprehensive overview, IEEE Access, vol. 7, pp. 114975–115001, 2019.

[11] Liserre M.: Design and control of an LCL-filter-based three-phase active rectifier, IEEE Trans. Ind. Appl., vol. 41, no. 5, pp. 1281–1291, 2005.

[12] Beres R. N.: A Review of Passive Power Filters for Three-Phase Grid-Connected Voltage-Source Converters," IEEE J. Emerg. Sel. Top. Power Electron., vol. 4, no. 1, pp. 54–69, 2016.

[13] Wang X.: Passivity-based design of passive damping for LCL-filtered voltage source converters, 2015 IEEE Energy Convers. Congr. Expo. ECCE 2015, pp. 3718–3725, 2015

[14] Yang Z.: Stability Investigation of Three-Phase Grid-Tied PV Inverter Systems Using Impedance Models," IEEE J. Emerg. Sel. Top. Power Electron., vol. 6777, no. c, pp. 1–13, 2020.

[15] Gharanikhajeh K.: A Harmonic Mitigation Technique for Multi-Parallel Grid-Connected Inverters in Distribution Networks," IEEE Trans. Power Deliv., pp. 1–1, Oct. 2021.

[16] Bianchi N.: Active power filter control using neural network technologies, IEE Proceedings-Electric Power Appl., vol. 150, no. 2, pp. 139–145, 2003.

[17] Berlingard Q.:RF performances at cryogenic temperature of inductors integrated in a FDSOI technology," Solid. State. Electron., p. 108285, 2022.

[18] Zhou S.:"An Improved Design of Current Controller for LCL-Type Grid-Connected Converter to Reduce Negative Effect of PLL in Weak Grid," IEEE J. Emerg. Sel. Top. Power Electron., vol. 6, no. 2, pp. 648–663, 2018.

[19] Yao W.: Design and Analysis of Robust Active Damping for LCL Filters Using Digital Notch Filters, IEEE Trans. Power Electron., vol. 32, no. 3, pp. 2360–2375, 2017

[20] Barsali S.: Benchmark systems for network integration of renewable and distributed energy resources; 2014.

[21] Jafarian M.: Grid Impedance Characterization To Provide a Robust Phase-Locked Loop Design for PV Systems," Proc. 2021 IEEE PES, ISGT Eur. 2021

[22] Sowa I.: Impedance-based analysis of harmonic resonances in HVDC connected offshore wind power plants," *Electr. Power Syst. Res.*, vol. 166, no. April 2018, pp. 61–72, 2019.

[23] Jia L.: An Adaptive Active Damper for Improving the Stability of Grid-Connected Inverters under Weak Grid," IEEE Trans. Power Electron., vol. 33, no. 11, pp. 9561–9574, 2018.